Engineering 2D Square Lattice Hubbard Models in 90° Twisted GeX/SnX (X = S, Se) Moiré Superlattices

Qiaoling Xu,[1,2,3,*] Ammon Fischer,[4,*] Nicolas Tancogne-Dejean,[4] Tao Zhang,[5,3] Emil Viñas Boström,[4] Martin Claassen,[6,†] Dante M. Kennes,[7,4,‡] Angel Rubio,[4,8,§] and Lede Xian[2,3,4,‖]

[1]College of Physics and Electronic Engineering, Center for Computational Sciences, Sichuan Normal University, Chengdu 610068, China
[2]Tsientang Institute for Advanced Study, Zhejiang 310024, China
[3]Songshan Lake Materials Laboratory, 523808 Dongguan, Guangdong, China
[4]Max Planck Institute for the Structure and Dynamics of Matter, Luruper Chaussee 149, 22761 Hamburg, Germany
[5]Department of Materials Science and Engineering City University of Hong Kong, Kowloon Tong, Hong Kong, SAR 999077, People's Republic of China
[6]Department of Physics and Astronomy, University of Pennsylvania, Philadelphia, Pennsylvania 19104, USA
[7]Institut für Theorie der Statistischen Physik, RWTH Aachen University and JARA-Fundamentals of Future Information Technology, 52056 Aachen, Germany
[8]Initiative for Computational Catalysis and Center for Computational Quantum Physics, Simons Foundation Flatiron Institute, New York, New York 10010, USA

(Received 26 March 2024; revised 17 December 2024; accepted 31 October 2025; published 15 December 2025; corrected 28 January 2026)

Because of the large-period superlattices emerging in moiré two-dimensional (2D) materials, electronic states in such systems exhibit low energy flat bands that can be used to simulate strongly correlated physics in a highly tunable setup. While many investigations have thus far focused on moiré flat bands and emergent correlated electron physics in triangular, honeycomb, and quasi-one-dimensional lattices, tunable moiré realizations of square lattices subject to strong correlations remain elusive. Here we propose a feasible scheme to construct moiré square lattice systems by twisting two or more layers of 2D materials in a rectangular lattice by 90°. We demonstrate the concept with twisted GeX/SnX (X = S, Se) moiré superlattices and calculate their electronic structures from first principles. We show that the lowest conduction flat band in these systems can be described by a square lattice Hubbard model with parameters which can be controlled by varying the choice of host materials, number of layers, and external electric fields. In particular, twisted double bilayer GeSe realizes a square lattice Hubbard model with strong frustration due to the next-nearest-neighbor hopping that could host unconventional superconductivity, in close analogy to the Hubbard model for copper-oxygen planes of cuprate high-temperature superconductors. The presented scheme uses 90° twisted 2D materials with rectangular unit cells as a promising platform for realizing the physical phenomena of square lattice Hubbard models, establishing a new route for studying its rich phase diagram of magnetism, charge order, and unconventional superconductivity in a highly tunable setting.

DOI: 10.1103/wcbz-lbr1

Subject Areas: Condensed Matter Physics, Strongly Correlated Materials

I. INTRODUCTION

The electronic Hubbard model [1–3] is ubiquitous in condensed matter research. In its original form it contains only two parameters: the electron hopping amplitude between adjacent sites (t) and a strong on-site interaction (U) between electrons of opposite spin. Despite its simplicity, the Hubbard model was employed early on to describe interaction-driven Mott metal-insulator transitions, with rich possibilities for magnetic order or quantum spin liquids at low temperatures [4,5]. Upon doping, the single band electronic Hubbard model is purported to

*These authors contributed equally to this work.
†Contact author: claassen@sas.upenn.edu
‡Contact author: Dante.Kennes@rwth-aachen.de
§Contact author: Angel.Rubio@mpsd.mpg.de
‖Contact author: xianlede@sslab.org.cn

support high-temperature superconductivity [6] and charge density waves [7,8], while strange metallicity and the pseudogap regime at finite temperatures have attracted considerable attention [9–11].

From a theoretical perspective, the apparent simplicity, yet intrinsic complexity, of the Hubbard model has captured the imagination of generations [12–14]. For many state-of-the-art methods of quantum many-body physics the (approximate) solution of the Hubbard model is viewed as an essential benchmark. Many complementary theoretical advances [7,11,15], such as dynamical mean-field theory, quantum Monte Carlo methods, renormalization group based approaches, or tensor network *Ansätze* try to draw a picture as complete as possible for the different regimes of their validity. For example, one-dimensional Hubbard models are often amendable to tensor networks [16,17], while high-dimensional Hubbard models can be well described by a dynamical mean field approach [18]. The most pertinent case of the two-dimensional fermionic Hubbard model can be addressed on bipartite lattices and at half filling using a quantum Monte Carlo description [19–22], but the superconducting state emerging at finite doping and frustration is difficult to capture with (numerically) exact methods beyond quasi-one-dimensional ladder geometries [23].

An alternative approach which has gained tremendous attention recently is to turn the problem upside down from computation to (quantum) simulation: Instead of a theoretical approach or classical computation, cold gases or other platforms [24] can provide highly controllable experimental simulations of the model system [25–32]. Here, the simulation of the (fermionic or bosonic) Hubbard model again constitutes one of the main goals and benchmarks. Much progress has been achieved concerning quantum magnetism in Hubbard-type models utilizing such a simulation approach, but yet many questions—e.g., the one of unconventional superconductivity—remain beyond the current simulation capabilities due to the ultralow temperatures that are necessary to access the corresponding energy scales [33].

With the recent rise of ultraclean and highly controllable two-dimensional materials, a new protagonist has entered the stage [34–38]. These materials are unique as they provide a high degree of tunability via heterostructure stacking, gating, and stress or strain, in a low disorder setting. Using stacking configurations that include either a relative twist between adjacent layers or an intrinsic lattice constant mismatch between layers of different materials, such moiré heterostructures have recently become one of the main areas of research focus in the field [24,39–49]. The large scale moiré interference pattern emerging at low twist angle or small lattice constant mismatches allows us to quench the kinetic energy scales promoting competing energy scales (such as the potential, spin-orbit, or phononic couplings). This concept has been explored extensively mainly in graphitic or transition metal chalcogenide materials and has raised the hope to realize many of the prototypical models of condensed matter physics [24,50–58]. In this work, we propose moiré materials engineering as an inroad to realize the prototypical square lattice Hubbard model with a nearest-neighbor hopping t and next-nearest-neighbor hopping t'. In contrast to the usual paradigm of using small twist angles, we study a bilayer system with each layer exhibiting a rectangular but only a slightly nonsquare unit cell rotated by 90° with respect to each other. The small lattice constant mismatch of the two sides of the rectangular unit cell combined with the rotation naturally generates a moiré pattern giving rise to the square lattice structure. This provides a pivotal materials-based platform to study unconventional superconductivity in a highly controlled two-dimensional materials platform allowing us to bridge the gap left open between theoretical approaches and quantum simulations in the future.

II. MOIRÉ SQUARE SUPERLATTICES FROM TWISTED RECTANGULAR LATTICES

A. General strategy

The natural way to obtain a 2D moiré square lattice is through twisting two layers of 2D materials with a square lattice unit cell. However, in practice, the number of 2D layered materials with square lattices that can be synthesized or exfoliated down to a monolayer or few layers in experiments is very limited. On the other hand, thin layers of 2D materials with rectangular lattices are more commonly studied, such as the group-IV monochalcogenides GeX/SnX (X = S, Se, Te) family [59], α-antimonene and β-tellurene [60–62], as detailed in Table II of the Supplemental Material [63]. Herein, we propose a general strategy to construct moiré square lattices based on the

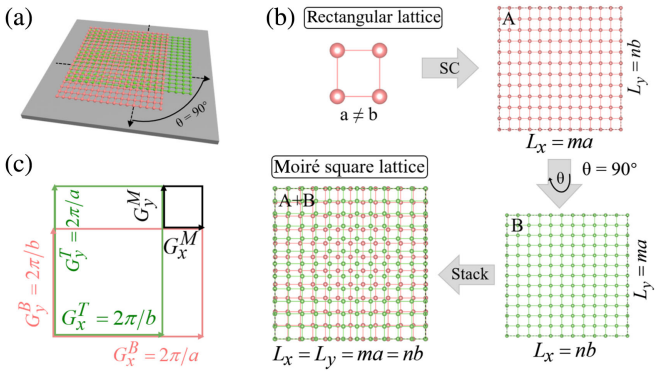

FIG. 1. General strategy of constructing moiré square lattices using 2D rectangular lattices. (a) Schematic illustration of the 90° twisted 2D layers. (b) Flow chart of the construction of the moiré square superlattice using 2D layers of rectangular lattices with different lattice constants a and b ($a \neq b$). (c) Brillouin zone of the 90° twisted rectangular lattices.

orthorhombic van der Waals (vdW) crystal structures with rectangular unit cell, as shown in Fig. 1.

Starting with two identical layers of 2D materials in a simple rectangular lattice with lattice constants $a \neq b$, one can twist one of the layers by 90° and stack it on top of the other layer. In this way, the lattice constants of the top and the bottom layers along the same axis are no longer equal and a moiré pattern will emerge. In the real space, the moiré wavelength L along the x and the y axes are both determined by the lattice mismatch between the original lattice constants a and b, i.e., $L_x = L_y = ma = nb$ (see Fig. 1). Therefore, the moiré period along the x and the y axes are equal and the resultant moiré pattern becomes a square lattice. In reciprocal space, as shown in Fig. 1(c), the reciprocal lattice vectors of the top or bottom layer and those of the moiré superlattice are connected by the following relation:

$$G_x^B - G_x^T = G_x^M, \tag{1}$$

where $G_x^B = 2\pi/a$, $G_x^T = 2\pi/b$, and $G_x^M = 2\pi/L$ are the reciprocal lattice vectors of the bottom layer, the top layer, and the moiré superlattice, respectively. Thus, real space lattice vectors a, b, and L satisfy the following equation:

$$\frac{1}{a} - \frac{1}{b} = \frac{1}{L}. \tag{2}$$

So L can be determined by the expression $L = [(1/a) - (1/b)]^{-1}$. The smaller the difference between the original lattices constants a and b, the larger the moiré period L. In practice, we will need to slightly strain the original lattice constants a and b such that we can construct a commensurate supercell containing only one moiré wavelength (see the Table I). This method of straining lattice constants to achieve commensurability was also very successful in the past to construct moiré triangular lattices using lattice mismatches of TMD heterostructures [45,52,68,69], as further demonstrated in Fig. S2 [63].

The fundamental design principles for constructing a square moiré lattice with isolated flat bands using rectangular unit cells are twofold. First, the chosen material should be semiconducting or semimetallic. This choice facilitates experimental control over the Fermi level and carrier concentration through gating. Moreover, the moiré potentials originated from the interlayer coupling are relatively weak, which are the most effective to the electronic states at the band edges. If the system is metallic, not all the electronic states around the Fermi level can be modified by the moiré potentials and those that are modified may be mixed with bulk metallic states, preventing the formation of clean, isolated flat bands needed for quantum simulations. Second, the material should have an appropriate lattice mismatch, with the resulting supercell lattice constant in the range of 10–100 Å. If the lattice mismatch is too large, leading to a small supercell period, the moiré potentials cannot effectively confine low-energy electronic states. For instance, materials like 1T'-WTe_2, despite having a rectangular unit cell, do not have sufficient lattice mismatch between the two lattice vectors, making it difficult to achieve isolated flat bands in a 90° twisted configuration. Conversely, if the lattice mismatch is too small, resulting in an overly large supercell lattice constant, maintaining structural homogeneity in experiments becomes challenging, which can disrupt flat band formation in the system (see Table II in the Supplemental Material) [63].

Compared to other possible approaches for generating superlattices with patterned substrates, our proposed system features moiré wavelengths below 10 nm, which are significantly smaller than the superlattice wavelengths reported in previous studies. For example, wavelengths close to 40 nm have been reported in the literature [70]. The reduced moiré wavelength leads to substantially stronger Hubbard interactions, which are inversely proportional to the wavelength. The stronger Hubbard interaction [1] facilitates the observation of correlation effects at experimentally accessible temperatures, broadening the range for tunability. Additionally, it is much easier to maintain structural homogeneity with a smaller supercell wavelength, which is also beneficial for experimental observations.

TABLE I. Parameters of constructing square lattices for 90° twisted bilayer GeX/SnX. (a), (b) Denote the two lattice constants in the primitive unit cell; (m, n) and (m', n') denote the supercell matrix for the top and the bottom layers, respectively; p and q denote the applied stress on lattice constants a and b, respectively, to achieve commensurability.

Materials	Unit cell (a, b)/Å	(m, n)	(m', n')	Scale (p, q)/%
GeS	(3.64, 4.29)	(7, 6)	(6, −7)	(0.5, −0.5)
GeSe	(3.83, 4.38)	(8, 7)	(7, −8)	(0.08, −0.08)
SnS	(3.98, 4.33)	(12, 11)	(11, −12)	(−0.2, 0.2)

B. 90° twisted bilayer GeX/SnX

We first apply this strategy to construct moiré square superlattices with 2D GeSe that have a rectangular lattice structure similar to that of black phosphorene [71]. The optimized atomic structures of 90° twisted bilayer GeSe is shown in Fig. 2. As expected, the twisted structure exhibits a moiré square superlattice with moiré lattice constant of 25.658 Å. The detailed structural parameters are summarized in Table I. The moiré structure mainly consists of two types of AA-like and two types of AB-like local stacking registries called AA^{α}, AA^{β}, AB^{α}, and AB^{β}. Each of these is uniquely identified by which atoms fall on top of each other in a top and side view as categorized in the right panels of Fig. 2. These four special stackings can be transformed into each other by translational sliding of one of the basal planes

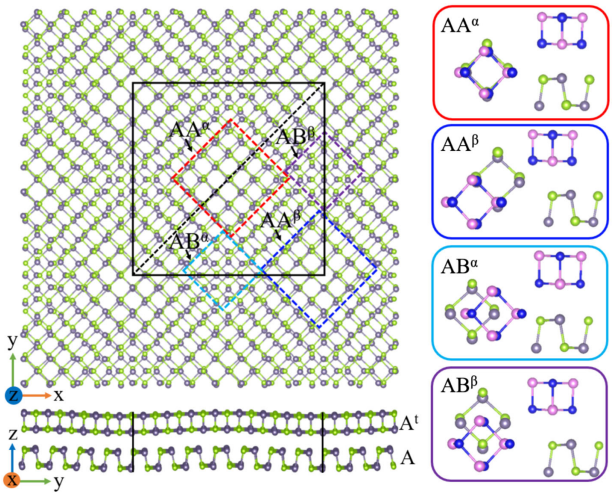

FIG. 2. Moiré structure of 90° twisted bilayer GeSe. The top and the side views of the atomic structure are shown in upper left and lower left panels, respectively. A^t in the side view is used to indicate the layer twisted by 90° with respect to the layer labeled as A. The moiré unit cell is indicated by black solid lines. The black dashed line represents the in-plane C_{2d} rotational axis. The top and the side views of the atomic structures of the local stacking configurations of AA$^{\alpha}$, AA$^{\beta}$, AB$^{\alpha}$, and AB$^{\beta}$ are shown in right panels. The Ge and the Se atoms are represented by green/blue and gray/pink balls, respectively.

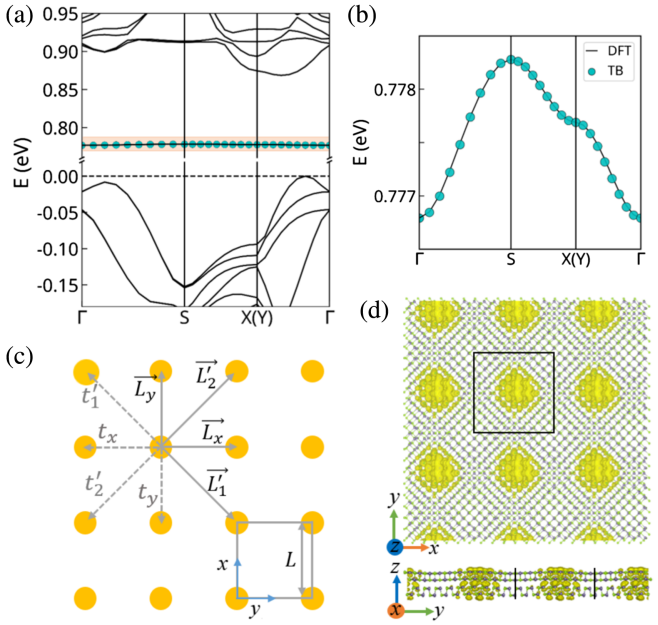

FIG. 3. Moiré flat bands of 90° twisted bilayer GeSe. (a) Low-energy band structure near the band edge. The dashed line indicates the Fermi level. (b) The enlarged band structure corresponding to the shaded region in (a), which shows the dispersion of the moiré flat band at the CBE. The black solid line and the cyan dots denote the results calculated with DFT and the effective TB model, respectively. (c) Schematic diagram of the square lattice effective TB model. (d) Top view (upper panel) and side view (lower panel) of partial charge density distribution in real space for the flat-band state at the CBE.

in the unit cell. Moreover, for such twisted bilayer structures, not only are the lattice constants along the two orthogonal directions equal, but the system also has an in-plane C_{2d} rotational symmetry along the diagonal direction of the moiré cell (see Fig. 2 dotted line), leading to equivalent electronic properties along the x and the y directions.

We then calculate the electronic band structures for a 90° twisted bilayer GeSe system using density functional theory calculations. The result is shown in Fig. 3(a). As expected, the band structure of the system along the X and the Y directions are identical. Because of the moiré modulation, an isolated flat band with ultrasmall bandwidth of 1.5 meV emerges at the conduction-band edges (CBE). The calculated charge density distribution of the flat band shows that these electronic states are localized at the AA$^{\alpha}$ regions, forming a square checkerboard pattern in real space [see Fig. 3(d)]. Based on these results, we model the flat band with a effective tight-binding (TB) model on a square lattice for which the Hamiltonian can be written as

$$\mathbf{H} = -\sum_{\langle i,j\rangle,\sigma} t_{ij} c_{i\sigma}^{\dagger} c_{j\sigma} + \sum_{\langle\langle i,j\rangle\rangle} t'_{ij} c_{i\sigma}^{\dagger} c_{j\sigma}, \tag{3}$$

where t_{ij} and t'_{ij} are the nearest-neighbor and the next-nearest-neighbor hopping amplitudes, respectively; $\langle\ldots\rangle$ and $\langle\langle\ldots\rangle\rangle$ represent the summation over the nearest neighbors and next-nearest neighbors, respectively; $c_{i\sigma}$ ($c_{i\sigma}^{\dagger}$) annihilates (creates) an electron at site i with spin $\sigma = \uparrow, \downarrow$. As the spin-orbit coupling for the flat band is negligible and thus the spins can be regarded as degenerate, using the notations shown in Fig. 3(c), the dispersion relation for one of the spin components can be written as

$$E(k) = 2t_x \cos(k_x L) + 2t_y \cos(k_y L) + 2t'_1 \cos(k_x L - k_y L) + 2t'_2 \cos(k_x L + k_y L), \tag{4}$$

where $t_x(t_y)$ denotes the nearest-neighbor hopping amplitude along the $x(y)$ direction and t'_1/t'_2 the next-nearest-neighbor hoppings along the diagonal directions; L denotes the lattice constant for the moiré square superlattice. As shown in Fig. 3(b), the fitted effective TB model gives almost identical band dispersion as the one calculated with DFT for the flat band at the CBE in the 90° twisted bilayer GeSe with $t_x = t_y$ (see Table II for values of the fitted parameters).

We further apply the strategy to other 2D group-IV monochalcogenides, namely GeS and SnS. Although the lattice constants of GeS and SnS are different from those of GeSe, the generality of the strategy ensures that the moiré structures end up as square superlattices. The atomic

TABLE II. Tight-binding parameters of the moiré flat bands for 90° twisted multilayer GeX/SnX fitted to DFT band structures.

Materials	t_x (meV)	t_y (meV)	t'_1 (meV)	t'_2 (meV)	t'_1/t_x (%)	t'_2/t_y (%)
2L-GeS	−6.054	−6.054	0.320	0.290	−5.2	−4.8
2L-SnS	−0.410	−0.410	−0.016	−0.012	3.9	2.9
2L-GeSe	−0.186	−0.186	−0.010	−0.027	5.3	14.5
2L-GeSe (0.1)*	−0.209	−0.169	−0.012	−0.029	5.7	17.1
2L-GeSe (0.2)*	−0.240	−0.158	−0.014	−0.032	5.8	20.2
2L-GeSe (0.3)*	−0.281	−0.153	−0.018	−0.037	6.4	24.1
3L-GeSe	−0.481	0.527	−0.010	−0.040	2.1	−7.6
4L (III-I)-GeSe	−0.947	0.967	−0.010	−0.081	1.1	−8.4
4L (II-II (AB-A^{t}B^t))-GeSe	0.188	0.172	−0.050	−0.028	−26.6	−16.3
4L (II-II (AB-B^{t}A^t))-GeSe	0.199	0.199	−0.036	−0.040	−18.1	−20.1

*The asterisk denotes results with external electric field. The value of the applied field is indicated in the parentheses and is given in units of eV/Å.

structures of the 90° twisted bilayer GeS and SnS are shown in Figs. 4(a) and 4(c) and the detailed parameters are listed in Table I. The moiré patterns of these systems are mainly formed by four local stacking domains similar to those of twisted bilayer GeSe. The corresponding DFT band structures are shown in Figs. 4(b) and 4(d). Similar to twisted GeSe, flat bands with narrow bandwidths of 48 and 3 meV appear at the CBE for twisted bilayer GeS and SnS, respectively. As shown in Fig. 4, these flat bands can be accurately fitted by the effective square lattice model described in Eq. (4) and we provide the hoppings amplitudes in Table II.

The moiré potentials induced by the interlayer hybridization variation across the superlattice period are mainly responsible for the formation of flat bands and charge density localization behavior at the square lattice sites. To illustrate this effect, we further perform two DFT calculations: one including only interlayer hybridization without atomic relaxation, and another with atomic relaxation fixed to that of the fully relaxed moiré bilayer, but with one layer removed to eliminate interlayer hybridization. The results are presented in Fig. S1 [63]. As shown in the figure, even with interlayer hybridization alone, ultraflat moiré minibands appear at the band edges. However, when interlayer hybridization is artificially removed by omitting one layer —while maintaining atomic reconstruction—this setup is insufficient to sustain flat bands at the band edges.

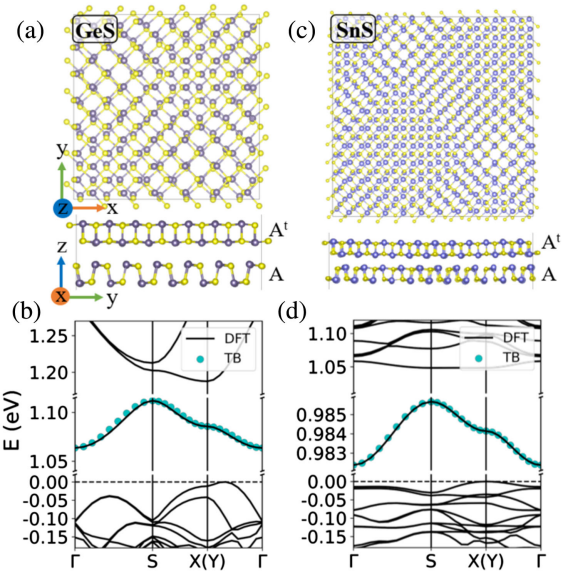

FIG. 4. Moiré flat bands of 90° twisted bilayer GeS and SnS. The atomic and the electronic structures of 90° twisted bilayer GeS (a), (b) and SnS (c), (d). The low energy flat bands at the CBE are fitted well by the effective TB model.

C. Γ-valley physics and building an effective continuum description

The flat moiré bands in 90° twisted bilayer GeX/SnX are shaped from the Γ-valley of the untwisted bilayers. Unfolding the full-fledged DFT band structure from the mini-Brillouin zone of the supercell to the primitive Brillouin zone of the pristine bilayers, see Fig. S7 [63] for the case of GeSe, reveals that the flat band of the conduction band minimum (CBM) is primarily constituted by a linear combination of Bloch states near the Γ point of the primitive Brillouin zone.

The unfolding analysis of Bloch states allows us to construct simplified analytical continuum models that describe the effective Γ-valley physics in 90° twisted bilayer GeX/SnX. Within aligned bilayers featuring the same local AA/AB$^{\alpha,\beta}$ stacking that appears in the twisted configuration, the bands at the Γ point are primarily shaped by the Ge p_z orbitals, see Supplemental Material Fig. S8 [63] for orbital-projected band structures of the respective bilayer configurations. The out-of-plane orientation of these orbitals leads to strong interlayer hybridization such that the energetically lowest states in the CBM are composed of bonding p_z states, whereas antibonding states are well separated in energy by ∼1.5 eV. Within

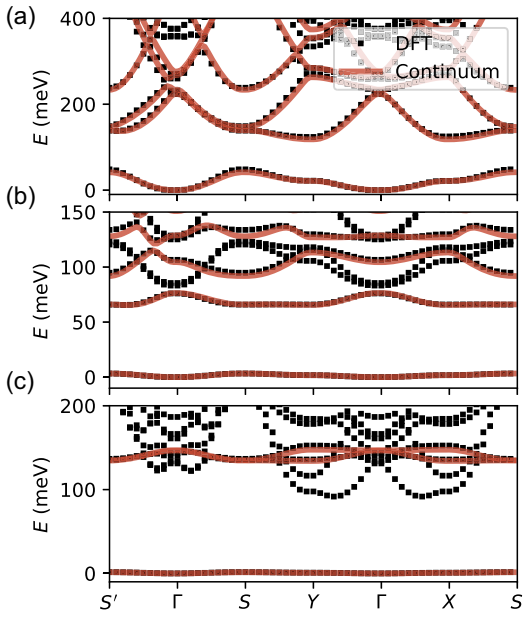

FIG. 5. Γ-valley continuum model for 90° twisted bilayer GeX/SnX. Continuum model and *ab initio* band structure for the square lattice moiré candidates (a) GeS, (b) SnS, and (c) GeSe.

our low-energy theory, we therefore only retain the bonding state at Γ, described by a $\boldsymbol{k}\cdot\boldsymbol{p}$ Hamiltonian [66,67] of the form

$$H(\boldsymbol{k}) = \frac{\boldsymbol{k}^2}{2m^*} + \boldsymbol{\Delta}(\boldsymbol{r}), \tag{5}$$

where m^* is the effective mass associated to the bonding p_z state of the GeX/SnX bilayers and $\Delta(\boldsymbol{r})$ is the moiré potential felt by the electrons in the CBM as a function of the real-space position $\boldsymbol{r}$ in the square moiré unit cell. The moiré potential is approximated in lowest harmonic Fourier expansion

$$\Delta(\boldsymbol{r}) = \sum_s \sum_{j=1}^{4} V(\boldsymbol{g}_j^s)\exp(i[\boldsymbol{g}_j^s\cdot\boldsymbol{r} + \psi_j^s]) + \text{H.c.}, \tag{6}$$

where $\boldsymbol{g}_j^s$ are the four reciprocal lattice vectors in shell s of the moiré Brillouin zone sorted by increasing distance $|\boldsymbol{g}_j^s|$. The in-plane rotational symmetry C_{2d} enforces $\Delta(\boldsymbol{r}) = \Delta(C_{2d}\boldsymbol{r})$, which restricts possible values of $(V(\boldsymbol{g}_j^s), \psi_j^s)$. Their magnitude is extracted by fitting to the *ab initio* DFT band structure and we give a detailed overview of symmetry-allowed continuum model parameters in the Supplemental Material [63].

Our results are shown in Figs. 5(a)–5(c). The continuum model is able to reproduce not only the flat moiré band, but also the higher energy bands in the conduction band manifold to good accuracy. For twisted bilayers of SnS and GeSe, additional bands admix to the higher-lying conduction bands, which do not originate from bonding states at Γ. However, these states do not constitute the moiré flat band.

D. 90° twisted multilayer GeX/SnX

The general strategy we proposed can also be applied to twisted multilayer GeX/SnX. With the additional layer degree of freedom, we can further engineer different flat band dispersions in a moiré square lattice. According to the review by Chang and Parkin [59] and the 2D materials database from high-throughput computational exfoliation of experimentally known compounds [72], the exfoliation energies of GeS, GeSe, and SnS are around 28–36 meV/Å^2, comparable to that of black phosphorene (30–38 meV/Å^2). Black phosphorene has been successfully exfoliated down to monolayer [73] and twisted monolayer-bilayer phosphorene has been fabricated in experiments [74]. With advancements in exfoliation techniques for 2D layers developed in recent years [75,76], we expect that all three systems (GeS, GeSe, and SnS) considered in this work can be further exfoliated down to monolayer in experiments. Currently, thin films of these materials with 2 to 4 layers have already been successfully obtained using liquid exfoliation methods. Taking the GeSe structures as typical examples, the multilayer moiré square superlattices can be generated by twisting monolayer on pristine bilayer (I-II), on pristine trilayer (I-III) or bilayer on bilayer (II-II) as shown in Figs. 6(a)–6(c). The untwisted layers remain in their natural AB stacking in their pristine

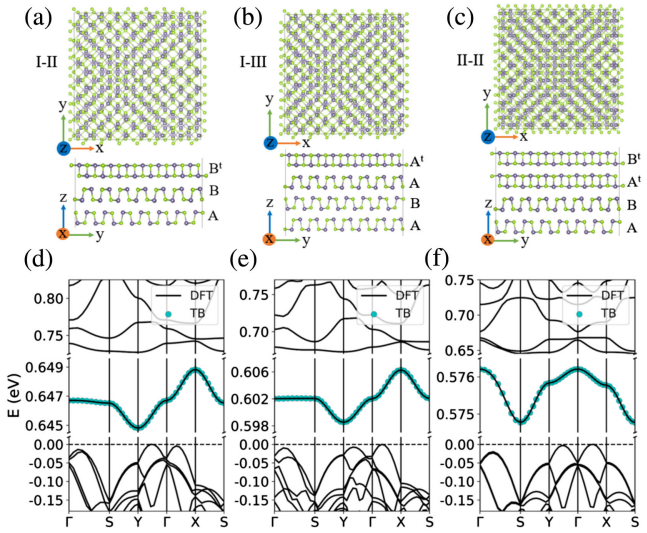

FIG. 6. Moiré flat bands of 90° twisted multilayer GeSe. (a)–(c) Top (upper panel) and side views (lower panel) of the atomic structures for the 90° twisted monolayer-bilayer (I-II), monolayer-trilayer (I-III) and AB-A^{t}B^t type of bilayer-bilayer (II-II) configurations, where AB, A^t and B^t indicate natural bilayer from bulk, 90° twisted A layer and 90° twisted B layer, respectively. The gray and green balls represent Ge and Se atoms, respectively. (d)–(f) The corresponding low energy band structures with fitting by the effective TB model.

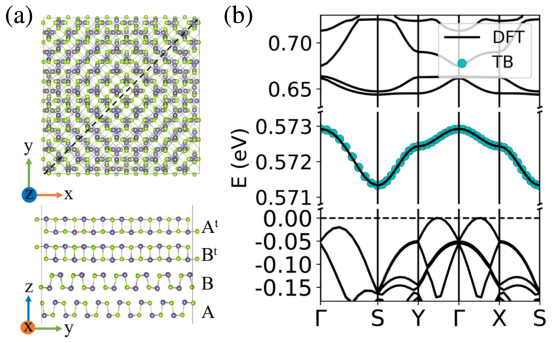

FIG. 7. 90° twisted double bilayer GeSe with symmetry. The atomic (a) and electronic structure (b) of the AB-B^{t}A^t type of twisted double bilayer GeSe where the C_{2d} symmetry around the diagonal axis of the moiré supercell is preserved. The low-energy flat band at CBE is fitted by the effective TB model shown in green markers.

bulk form. The corresponding band structures for these moiré superlattices are given in Figs. 6(d)–6(f). Similar to the twisted bilayer systems, all of these twisted multilayer structures exhibit very flat minibands appearing at the CBE with bandwidths of 4, 7, and 1.4 meV, respectively. In these three types of twisted multilayer structures, the in-plane C_{2d} rotational symmetry is broken and the electronic properties along the x and the y axis are not equivalent. Nevertheless, the bottom moiré flat bands at the CBE in the twisted multilayer superlattices can also be described by the simple square lattice effective model given by Eq. (4) with different values for t_x and t_y (see fitted parameters in Table II). Therefore, with ultraflat bands and inequivalent hoppings along the x and the y axis, these moiré systems can be used to realize anisotropic square lattice Hubbard models.

For twisted multilayer systems with even number of layers, the in-plane C_{2d} rotational symmetry can be restored by designing the twist stacking. For example, in the twisted double bilayer system, by twisting the top two layers by 90° with respect to the bottom two layers, one can obtain a moiré square superlattice in the AB-A^{t}B^t type of stacking [Fig. 6(c)]. By further flipping the top two layers up side down in the AB-A^{t}B^t type of twisted double bilayer superlattice, one obtains the AB-B^{t}A^t type of moiré superlattice [Fig. 7(a)]. While the in-plane C_{2d} rotational symmetry along the diagonal direction of the supercell is absent in the AB-A^{t}B^t type of moiré superlattice, it is restored in the AB-B^{t}A^t type. As shown in Fig. 7(b), the band dispersion for the AB-B^{t}A^t type twisted double bilayer GeSe along the x and the y directions are exactly the same due to the symmetry in the system. In particular, the lowest moiré flat band at the CBE can be fitted to the effective TB model with $t_x = t_y$ (see Table II). Interestingly, for twisted multilayer moiré square superlattices, the next-nearest-neighbor hopping versus nearest-neighbor hopping ratio t'/t is generally larger than that of the twisted bilayer. For the AB-B^{t}A^t type twisted double bilayer GeSe, this value reaches ∼20%.

E. Near 90° twisted GeX/SnX

Stacking two layers at a slightly varying twist angle of $90° + \Delta\theta$, a rhombus-shaped moiré pattern forms, similar to those that observed in the system with a perfect 90° twist. In reciprocal space, as shown in Fig. 8(c), the relationship between the reciprocal lattice vectors of the top and bottom layers and those of the moiré superlattice is given by

$$\boldsymbol{G}_i^B - \boldsymbol{G}_i^T = \boldsymbol{G}_i^M, (i = 1, 2), \tag{7}$$

where $\boldsymbol{G}_{1,2}^B$, $\boldsymbol{G}_{1,2}^T$, and $\boldsymbol{G}_{1,2}^M$ are the reciprocal lattice vectors of the bottom layer, top layer, and moiré superlattice, respectively. Thus, the real space lattice vector $\boldsymbol{L}_{1,2}$ can be derived from the relationship $\boldsymbol{G}_i^M \cdot \boldsymbol{L}_i = 2\pi$ $(i = 1, 2)$. The angle θ between $\boldsymbol{G}_1^M$ and $\boldsymbol{G}_2^M$, the angle φ between $\boldsymbol{L}_1$ and $\boldsymbol{L}_2$, and the magnitudes of each vectors for near 90° twisted GeSe are listed in Table III of Supplemental Material [63]. Using the small angle approximation, one can show that when the twist angle θ is deviated from 90° by $\Delta\theta$, the angle φ between the superlattice vectors will deviate from 90° by $\Delta\varphi = [(a + b)/(b - a)]\Delta\theta$, where a, b are the two primitive cell lattice constants. Therefore, a slight deviation of the twist angle from 90° results in a magnified deviation of the angle between the supercell lattice vectors from 90°. The magnified ratio is proportional to the sum of the

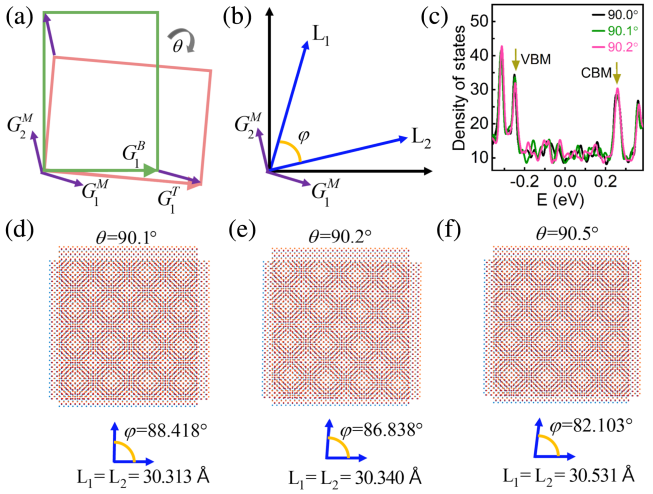

FIG. 8. Nearly 90° twisted bilayer GeSe. (a) Brillouin zone of nearly 90° twisted rectangular lattices with the reciprocal lattice vectors G_1^M and G_2^M. (b) Relationship between the reciprocal lattice vectors and real space supercell lattice vectors. (c) Density of states of twisted bilayer GeSe at different twist angles near 90° using DeepH. (d)–(f) The atomic structures of 90.1, 90.3, 90.5° twisted GeSe in real space with their estimated supercell lattice vectors L_1 and L_2 and the angle between them shown in the lower panels.

primitive cell lattice constants, $a + b$, divided by the lattice mismatch, $b - a$. Nevertheless, for 2D materials that do not have an extremely small lattice mismatch between the two unit cell lattice constants, if the twist angle deviation is limited to a small subdegree scale as can be achieved in experiments [69], the shape of the superlattice will not be distorted too much from a perfect square. For the case of near 90° twisted GeSe, the corresponding moiré superlattice structures in real space are shown in Figs. 8(d)–8(f). As shown in these figures, the moiré pattern exhibits minimal variation for twist angles of 90.1°, 90.2°, and 90.5°, indicating a high degree of structural stability across these slight angular deviations.

To evaluate the effect of angle deviation on electronic properties, we perform additional calculations for these systems. To account for small twist angle deviations without being constrained by the commensurate condition, we use two large flakes of GeSe stacked at a twist angle close to 90° in real space for each system. The size of each flake is larger than 24 nm, which is sufficient to mimic the bulk. Since each system contains 21 952 atoms, density functional theory (DFT) methods become impractical; thus, we employed deep learning-assisted electronic structure calculations (see Appendix for details). The effectiveness of this approach is validated by the band structure calculation of the periodically twisted 90° GeSe bilayer presented in Fig. S3 of Supplemental Material [63]. The calculated densities of states (DOS) for structures with slight deviations from 90° are shown in Fig. 8(c). These results indicate that the position and the width of the conduction band minimum peak in the DOS, corresponding to the flat band, remain nearly unchanged when the twist angle deviates from 90° by up to 0.2°, suggesting that small angle deviations have minimal impact on the electronic structure.

F. Correlation-driven antiferromagnetic order in 90° twisted GeX/SnX moiré superlattices

In flat bands, electronic interactions can dictate electronic properties and give rise to emergent phases in a highly-tunable setting. In order to gain insight into the role of electronic correlations, we complemented our DFT simulations by DFT + U + V simulations, in which an on-site effective Hubbard U and an intersite interaction V (for the localized Wannier orbitals constructed from the DFT flat bands) are added to the DFT Hamiltonian. These effective electronic parameters are evaluated *ab initio* (see the Appendix for more details) in order to determine the ground state of the system when static correlation effects are included. To this end, we performed several DFT + U + V calculations at half filling of the flat band in the unit cell of twisted GeSe, as well as in doubled 2×1 supercells, in order to determine the lowest-energy configuration and allow for collinear and Néel antiferromagnetic order. As expected for a square-lattice Hubbard model with weak frustration, we found that the system exhibits an antiferromagnetic instability at half filling [77], with the Néel antiferromagnetic order being lower than the collinear antiferromagnetic order. However, in contrast to conventional antiferromagnetic insulators composed of atomic orbitals, the effective magnetic moments extend over the charge accumulation regions in the moiré unit cell. Each localized Wannier state is found to host a finite magnetization. The Wannier states obtained at the DFT level for the 2×1 supercell with Néel antiferromagnetic order of GeSe are shown in Figs. 9(a) and 9(b) and the corresponding magnetization, obtained once on-site and intersite interactions are included is shown in Fig. 9(c). The obtained effective electronic parameters give an on-site interaction $U_{\text{eff}} \approx 1.45$ meV, corresponding to $U/t \simeq 7.8$, and a ratio of the intersite interaction to the on-site effective one to be $U_{\text{eff}}/V \approx 10$.

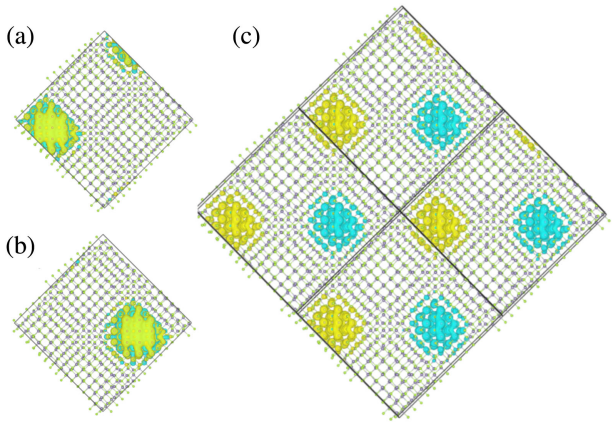

FIG. 9. Electronic ground states of the moiré flat bands in the 90° twisted bilayer GeSe with correlations. (a)–(b) Wannier states corresponding to the two flat bands of a checkerboard 2×1 supercell of twisted bilayer GeSe. (c) The corresponding magnetization density obtained from DFT + U + V at half filling.

G. Realizing *d*-wave superconductivity via 2D heterostructure engineering

Having established a tunable moiré realization of a square-lattice Hubbard antiferromagnet at half filling, gate-induced doping and materials compositions now open up new routes for testing longstanding questions regarding the phase diagram of square lattice Hubbard models, mechanisms for unconventional superconductivity, intertwined charge orders and the role of frustration [11,12,14]. For strong interactions, prior theoretical studies of the doped square lattice Hubbard model indicate a close competition between charge/spin stripe order and a uniform d-wave superconducting phase, which give way to a Fermi liquid at dilute filling [14]. However, more exotic states such as pair-density wave order have been proposed as well [11,78–80]. Electronic frustration via next-nearest-neighbor hopping terms t' plays a key role. While the unfrustrated doped Hubbard model at strong coupling with solely

nearest-neighbor hoppings was found by multiple numerical methods to favor stripe order without superconductivity [7,8,81] near optimal doping, prior theoretical work indicates that a finite next-nearest-hopping t' can stabilize d-wave superconductivity [8,82–87].

Here, we elucidate this question by addressing electronic correlations by unbiased functional renormalization group (FRG) [88,89] calculations of twisted bilayer GeSe starting from the *ab initio* electronic parameters. The FRG smoothly connects the noninteracting model to an effective low-energy theory by successively integrating out high-energy degrees of freedom above a flowing energy cutoff $\Lambda = \infty \to 0$ such that quantum fluctuations are systematically included in the effective two-particle interaction vertex. By perturbatively expanding possible scattering processes, the FRG allows for an unbiased treatment of electronic order and symmetry-breaking transitions in the pairing, charge, and magnetic channel. A divergent interaction in one of the channels at scale $\Lambda_c \sim T_c$ indicates the transition to a symmetry-broken electronic phase, see the Method section for details. This renders FRG a suitable method to analyze the competition of antiferromagnetic order and superconductivity in the frustrated $t - t'$ low-energy models of 90° twisted GeX/SnX moiré superlattices.

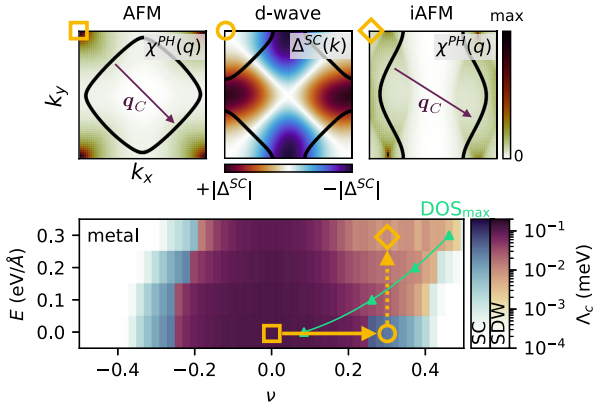

FIG. 10. FRG phase diagram of 90° twisted GeSe in the presence of an external displacement field E. The phase diagram shows the critical scale $\Lambda_c \sim T_c$ of the leading Fermi surface instability and indicates regimes of spin density wave order (SDW, red), superconductivity (SC, blue) and unordered metallic regimes. At half filling ($\nu = 0$), the system features antiferromagnetic order (yellow square) and the particle-hole susceptibility $\chi^{\mathrm{PH}}(\boldsymbol{q})$ is peaked at the commensurate nesting vector $\boldsymbol{q}_C = (\pi, \pi)$. Upon electron (hole) doping, the nesting conditions are weakened such that AFM fluctuations give rise to d-wave superconductivity (yellow circle). In the presence of an external displacement field, the Fermi surface becomes anisotropic and is stretched in the $\hat{y}$ direction, which weakens superconductivity and strengthens incommensurate AFM order (iAFM, yellow diamond), whose anisotropy axis follows the leading bosonic momentum transfer $\boldsymbol{q}_C$. The green line indicates the van-Hove singularity on the electron-doped side that tunes to larger electron densities as the displacement field is increased.

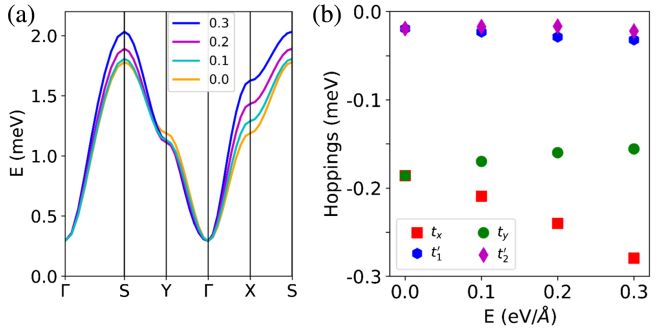

FIG. 11. Electric field tuning of moiré flat bands in 90° twisted bilayer GeSe. (a) The flat bands at the CBE under various vertical electric field (E) with the value of 0.0, 0.1, 0.2, and 0.3 eV/Å. (b) The effective model fitting parameters as a function of the electric field.

The results of the FRG study are summarized in Fig. 10. The phase diagram shows the critical scale Λ_c of the leading Fermi surface instability and indicates regimes of spin density wave order (SDW, red), superconductivity (SC, blue), and metallic regimes without electronic order. At half filling ($\nu = 0$, yellow square), the FRG predicts an extended range of antiferromagnetic (AFM) order that is driven by nesting between the approximate C_{4v}-symmetric Fermi surface sheets with vector $\boldsymbol{q}_C = (\pi, \pi)$ in line with the DFT + U + V analysis provided in the previous paragraph. The particle-hole susceptibility $\chi^{\mathrm{PH}}(\boldsymbol{q})$ in the AFM phase and the respective Fermi surface (black line) are shown in the upper panel of Fig. 10. Upon electron (hole) doping, the nesting conditions are weakened such that AFM order eventually gives way to d-wave superconductivity at $\nu \sim 0.3$ (yellow circle), driven by fluctuations of the nearby AFM state. The superconducting order parameter $\Delta^{\mathrm{SC}}(\boldsymbol{k})$ is shown in the upper panel of Fig. 10 and exhibits gapless points whenever the Fermi surface intersects with zeros of the order parameter.

While we exemplified the emergence of d-wave superconductivity in twisted bilayer of GeSe, we stress the generality of our approach suggesting similar correlated states to emerge in the family of other 90° twisted GeX/SnX moiré superlattices. To this end, the materials parameterized in Table II provide a route to simulate the role of frustration in the square lattice Hubbard model in an experimental setting via heterostructure composition. Notably, four-layer twisted GeSe configurations most closely mirror weak frustration $|t'/t| \approx 0.2$ representative of cuprate high-temperature superconductors [13,23]. In contrast to cuprates, electron and hole doping away from half filling are flipped by virtue of t' and t carrying the same sign.

H. Simulating the competition of stripe order vs *d*-wave superconductivity via external displacement fields

Interestingly, the proposed moiré realization of a two-dimensional Hubbard model can also serve as a simulator to explore competing ground states at finite filling. For instance, while the unfrustrated Hubbard model at $1/8$ doping was found by multiple methods to favor a period-8 stripe phase without superconductivity [7,8], the stability of stripe order, variations of its period, and the onset of d-wave superconductivity for variations of either filling or frustration has attracted much attention [8,82–85].

We propose that our design principle for 90° twisted GeX/SnX moiré superlattices allows us to investigate this question by tuning the anisotropy of the Fermi surface *in situ* via the application of external displacement fields—favoring either striped-AFM order or d-wave superconductivity. Figure 11(a) shows the low-energy flat bands of the CBE of twisted bilayer GeSe for four different strengths of the external electric field of 0.0, 0.1, 0.2, and 0.3 eV/Å. For finite displacement field, the in-plane C_{2d} rotational symmetry is broken, leading to an energetic offset between the X point and the Y point of the moiré Brillouin zone. The strength of the anisotropy is steered by the strength of the displacement field, while the overall bandwidth of the moiré flat band is only slightly altered. We summarize the effective hoppings parameters for the anisotropic $t-t'$ models of twisted bilayer GeSe in Table II and show their displacement field dependence in Fig. 11(b). For experimentally relevant field strengths, the effective hopping amplitudes can be tuned over a wide range, highlighting the flexibility of our engineering approach in tuning electronic properties in 90° twisted moiré superlattice.

The electronic structure engineering also has profound impact on the correlated electronic phases and the competition between striped AFM order and d-wave superconductivity as shown in Fig. 10. In the presence of an external displacement field, the Fermi surface becomes anisotropic and is stretched in the $\hat{y}$ direction (yellow diamond). This weakens d-wave superconductivity and strengthens incommensurate AFM order (iAFM). Maxima of the particle-hole susceptibility $\chi^{\mathrm{PH}}(\boldsymbol{q})$ in this phase are shifted away from (π,π), which indicates the formation of striped-AFM order whose anisotropy axis follows the leading momentum transfer $\boldsymbol{q}_C$. To this end, the formation of striped AFM order on the electron-doped side is facilitated by the emergence of a tunable van-Hove singularity on the electron-doped side (green line) that tunes to larger electron densities as the displacement field is increased. Regions of superconducting order are instead displaced to larger electron (hole) doping, however, survive even in the presence of anisotropies at larger electron (hole) dopings. Therefore, we argue that 90° twisted GeX/SnX moiré superlattices provide an ideal testbed to tune between striped AFM order and d-wave superconductivity via displacement field control of the anisotropy in the system.

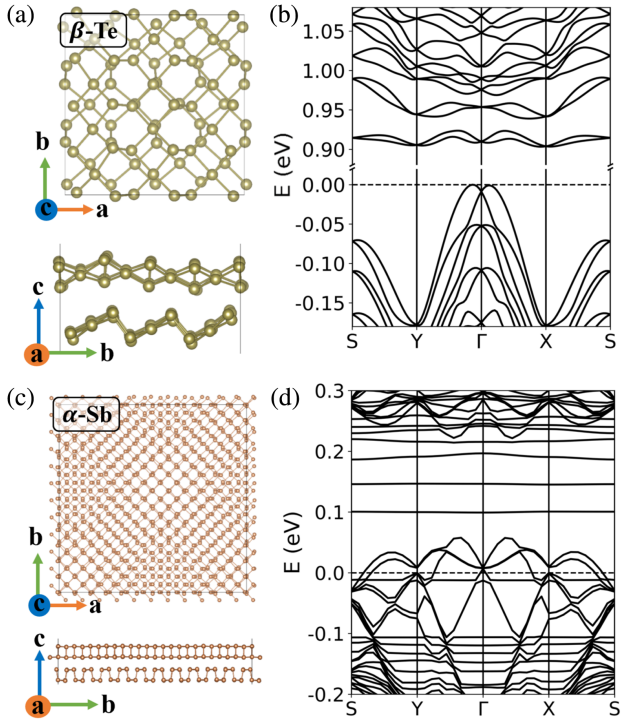

FIG. 12. The atomic (a),(c) and the electronic structures (b),(d) of 90° twisted bilayer β-Te and α-Sb, respectively. The dashed line represents the Fermi level.

I. Other potential material candidates

The general strategy we propose for constructing moiré square superlattices can also be applied to other 2D materials with rectangular lattices. We specifically investigate moiré square superlattices formed by twisting β-tellurene and α-antimonene. Both β-tellurene and α-antimonene have been successfully synthesized or exfoliated down to monolayers in experiments [60–62], making them viable candidates for fabricating 90° twisted bilayer or multilayer systems. The atomic structures and calculated band structures of 90° twisted bilayer β-tellurene and α-antimonene are shown in Fig. 12. The moiré square lattices of these systems have lattice constants of 17 and 52 nm, respectively. As shown in Figs. 12(b) and 12(d), isolated flat bands emerge at the band edges of both systems, with bandwidths of less than 20 meV for β-tellurene and 1.5 meV for α-antimonene. These properties suggest that these systems could be utilized to explore Hubbard model physics on a square lattice. In addition to the materials presented in this study, we identify more than 40 other potential 2D material candidates with rectangular lattices, listed in Table III. These materials have exfoliation energies comparable to that of black phosphorene, making them suitable for exfoliation from bulk to fabricate 90° twisted layers. Furthermore, they possess lattice constants that result in moiré superlattice wavelengths between 2 and 10 nm. This range is ideal for the formation of flat bands

TABLE III. Other potential 2D materials candidates for realizing square lattice Hubbard model in 90° twisted systems. (a),(b) denote the two lattice constants in the primitive unit cell; E_b represents the binding energy calculated using rVV10 functionals from MC2D database [72]; E_g represents the band gap obtained from PBE functionals; the moiré period L is estimated by $L = [(1/a) - (1/b)]^{-1}$; and the "3D parent ID" column lists the identification numbers of the corresponding 3D parent compounds for each 2D layered material.

Materials	Unit cell(a), (b)/Å	E_b/meV/Å^2	E_g/eV	L/Å	3D parent ID
SnSe	(4.15, 4.44)	35.72	0.96	63.53	COD (9008786)
GeTe	(4.22, 4.37)	…	0.80	122.00	ICSD (638005)
β-PbO	(4.87, 5.55)	27.20	2.53	39.62	COD (2310433)
SnO	(4.53, 5.31)	28.40	2.10	30.83	ICSD (424729)
MoO_3	(3.71, 3.87)	26.64	1.53	87.08	ICSD (80577)
$PdSeO_3$	(6.53, 7.27)	29.70	0.40	64.15	ICSD (415955)
HfNBr	(3.57, 4.12)	18.17	2.13	26.62	COD (1532008)
ZrNI	(3.75, 4.14)	20.20	1.28	39.57	ICSD (36119)
ZrNBr	(3.62, 4.14)	18.29	1.80	28.45	ICSD (27393)
TeO_2	(5.32, 5.74)	54.8	2.30	72.70	COD (1011183)
PdI_2	(6.9, 8.36)	33.17	1.05	39.38	ICSD (25120)
PtI_2	(6.88, 8.52)	31.88	1.35	35.63	ICSD (60760)
ScOBr	(3.57, 3.98)	17.28	3.07	34.43	COD (2206575)
InOBr	(3.64, 4.14)	17.30	2.26	30.41	ICSD (24059)
InOCl	(3.56, 4.17)	…	2.59	24.33	ICSD (24058)
InTeBr	(7.56, 8.39)	19.65	2.26	76.87	COD (1524712)
InTeI	(7.77, 8.63)	19.03	1.73	78.00	COD (1525202)
SbOCl	(9.44, 10.94)	45.48	2.05	68.64	ICSD (24751)
TiNBr	(3.36, 3.95)	20.10	0.60	22.49	ICSD (27395)
NbO_2I	(3.77, 3.91)	21.53	0.81	109.46	ICSD (418061)
Nb_2SiTe_4	(6.34, 7.87)	28.10	0.56	32.66	ICSD (81416)
Nb_2GeTe_4	(6.47, 7.9)	27.47	0.47	35.76	ICSD (81417)
$ZnAs_2O_4$	(4.54, 4.99)	27.98	3.39	49.56	COD (9001071)
W_4PBr_{11}	(10.45, 11.93)	18.45	0.56	83.87	COD (4341586)
W_4PCl_{11}	(9.94, 11.42)	17.86	0.57	77.03	ICSD (422269)
$Re_2S_2O_{13}$	(8.38, 9.77)	18.25	2.10	58.85	COD (4324293)
$LiBiO_2$	(4.73, 5.27)	38.68	2.27	46.66	ICSD (25385)
KAs_2F_7	(7.21, 8.41)	31.27	4.19	50.63	ICSD (36332)
Li_2ZnBr_4	(6.5, 7.73)	44.93	3.47	40.87	COD (1517836)
Nb_2PbO_6	(4.81, 5.28)	21.89	1.89	53.93	COD (2101515)
$AlBiCl_6$	(11.89, 17.92)	16.52	3.59	35.36	ICSD (414261)
CdP_2O_{10}	(8.63, 10.22)	27.94	1.36	55.39	COD (9015952)
Hg_2TeBr_3	(10.22, 13.47)	31.49	1.66	42.39	ICSD (417407)
Na_2ZnCl_4	(6.4, 8.05)	41.28	4.16	31.10	ICSD (402063)
Na_2PSe_3	(8.0, 11.76)	35.33	1.75	25.05	ICSD (415240)
$NaNbCl_6$	(6.33, 6.82)	18.85	2.21	88.92	ICSD (36518)
$NaGaH_4$	(6.37, 6.98)	25.36	4.44	73.04	ICSD (67309)
KAuS	(6.53, 7.85)	42.52	1.68	38.91	COD (1510204)
KAuSe	(6.85, 8.1)	39.08	1.49	44.29	COD (1510205)
KC_2N_3	(6.93, 8.43)	32.53	4.37	38.88	ICSD (411930)
KO_3Cl	(4.65, 5.57)	23.89	5.40	28.09	COD (2310654)
KCN_7	(6.39, 8.09)	23.87	3.50	30.42	COD (4103810)
K_2PdAs_2	(5.94, 6.39)	44.36	0.54	83.71	ICSD (32009)
KSb_2F_7	(7.52, 8.21)	25.87	3.93	88.94	COD (4343786)
K_2SiAs_2	(6.44, 6.98)	36.97	0.96	83.78	ICSD (40426)
K_2SiP_2	(6.09, 6.79)	41.24	1.19	59.21	ICSD (36367)
K_2WSe_4	(9.73, 12.43)	38.92	1.58	44.83	COD (2005921)
K_3InP_2	(6.77, 7.57)	37.82	0.74	63.73	ICSD (300141)
K_2GeSe_4	(8.13, 9.11)	26.09	1.78	75.50	ICSD (78828)
K_2GeTe_4	(8.34, 10.21)	24.63	0.89	45.59	ICSD (38341)

while maintaining structural homogeneity in experimental systems.

III. CONCLUSIONS

Our work proposes a general scheme to use rectangular-lattice 2D van der Waals materials to construct moiré square superlattices. We predict that moiré heterostructures of 90° twisted bilayers and multilayers of the rectangular-lattice transition-metal dichalcogenide family (Ge/Sn)(S/Se) can provide a platform to realize the paradigmatic square-lattice Hubbard model with repulsive interactions in a tunable setting. In this set of compounds, layer composition grants a twofold handle to tune electronic frustration and drive the material into a regime with narrow square-lattice moiré bands dominated by strong Coulomb interactions. Focusing on 90° rotated bilayers of GeSe, we computed the strength of Coulomb interactions and predict the formation of a paradigmatic square-lattice Mott insulator with Néel order at half filling. Combined with gate-tunable carrier doping, this suggests that 90°-twisted (Ge/Sn)(S/Se) can serve as an experimental solid-state platform to simulate the phase diagram of the copper-oxygen planes of cuprate high-temperature superconductors, to provide new experimental insights into the nature of the pseudogap, the role of electronic frustration, and competing and intertwined superconducting and density wave orders.

Note added.—After completing this work we came across a related paper by Eugenio and collaborators [90]. Their work proposes realizing a similar square lattice Hubbard model with frustration (or the $t - t' - U$ model) using a twisted square homobilayer, based on their model only calculations.

ACKNOWLEDGMENTS

L. X. and Q. X. acknowledge the support by the National Key Research and Development Program of China (Grant No. 2022YFA1403501), the National Natural Science Foundation of China (Grants No. 12504218 and No. 12474174), and the Max Planck Partner group programme. D. M. K. acknowledges funding by the Deutsche Forschungsgemeinschaft (DFG, German Research Foundation) within the Priority Program SPP 2244 "2DMP"—443274199 and under Germany's Excellence Strategy—Cluster of Excellence Matter and Light for Quantum Computing (ML4Q) EXC 2004/1–390534769. M. C. acknowledges support by the U.S. Department of Energy (DOE), Office of Basic Energy Sciences, under Award No. DE-SC0024494. We acknowledge computational resources provided by RWTH Aachen University under Project No. rwth0763. This work was supported by the Max Planck-New York City Center for Nonequilibrium Quantum Phenomena. This work was supported by the European Research Council (ERC Synergy Grant Agreement No. 101167294 (UnMySt)), the Cluster of Excellence "CUI: Advanced Imaging of Matter" of the Deutsche Forschungsgemeinschaft (DFG)—EXC 2056—Project ID 390715994 and Deutsche Forschungsgemeinschaft (DFG) -SFB-925–Project No. 170620586. The Flatiron Institute is a division of the Simons Foundation.

DATA AVAILABILITY

The data are not publicly available. The data are available from the authors upon reasonable request.

APPENDIX: MODEL AND COMPUTATIONAL APPROACHES

1. Density functional theory calculations

The present calculations are done within the framework of density functional theory using the plane-wave pseudopotential approach performed in the VASP code [91]. The electron-ion interactions can be described by the projector augmented wave (PAW) pseudopotentials [92]. Configurations of $4s^2 4p^2$ for Ge, $5s^2 5p^2$ for Sn, $3s^2 3p^4$ for S and $4s^2 4p^4$ for Se are considered as valence electrons. We use the Perdew-Burke-Ernzerhof (PBE) parametrization of the generalized gradient approximation [93] as the exchange correlation functional. We calculate the equilibrium lattice parameters of GeS in the bulk phase and found that the DFT-TS vdW functionals [94] provide better agreement with the experimental values [71] within less than 1% errors. The DFT-TS vdW functional is then adopted for all calculations. A plane-wave basis set with an energy cutoff of 400 eV and a $1 \times 1 \times 1$ momentum grid are used to characterize the ground state and the mechanical relaxation. Our calculations are fully relaxed (with respect to all the atoms), which is known to be important in other moiré systems to avoid artificial effects stemming from unrelaxed structures. The relaxation procedure ensures that the force on each atom converges to values smaller than 0.01 eV/Å. A long z-direction auxiliary vacuum region larger than 15 Å is added to avoid the artificial interaction between the periodic slabs. As spin-orbit coupling (SOC) is found to have negligible effects on the flat bands calculated for the systems, we exclude SOC in the calculations.

2. Deep-learning assisted electronic structure calculation

The electronic structure calculation for the nonperiodic moiré supercell slab has been encapsulated in the DeepH package [95]. The key idea is to employ machine learning to study the relationship between the Hamiltonian matrix and material structure, and then to make predictions for new systems. By constructing hundreds of small structures, a corresponding database of Hamiltonian is obtained using

DFT methods and subsequently trained by neural networks. Thereafter, trained network models can be used to predict the band structure of larger structures. To train the DeepH model for moiré twisted GeSe bilayers, we prepared datasets (625 configurations) from zero-twist-angle $5 \times 5 \times 1$ bilayer supercells by shifting the top layer within the 2D plane and inserting random perturbations to each atomic site, based on the relaxed primitive GeSe bilayer. Adopting the same constructing manner, we have also built a group (82 configurations) of unrelaxed 90° twisted bilayer GeSe. All these dataset structures were calculated using localized pseudoatomic orbitals (PAOs) and pseudopotentials as implemented in the OPENMX code [96], due to the localization ability of the basis. The exchange-correlation functional, treated by the generalized gradient approximation of the Perdew-Burke-Ernzerhof form [93], and norm-conserving pseudopotentials [97], and the DFT-D3 method corrected van der Waals interaction [98] were used in the calculations. The basis sets for the two elements in the system were chosen as Ge7.0-$s^3p^2d^2$ (RC = 7.0 Bohr) and Se7.0-$s^3p^2d^2$, which include 19 atomic-like basis functions. The energy cutoff was set to 300 Ry in real space for numerical integration and solving the Poisson equation. A $7 \times 6 \times 1$ and $2 \times 2 \times 1$ mesh of k-points were adopted in preparing the datasets of $5 \times 5 \times 1$ GeSe bilayer and 90° twisted bilayer GeSe, respectively. The convergence criterion was set as a total energy difference of less than 4×10^{-7} Hartree. During the training step, a message-passing neural network (MPNN) implemented in the PyTorch-Geometric Python library [99] was used to represent the Hamiltonian matrix, where the vertices, edges, and edge embeddings represent atoms and atom pairs, and Hamiltonian matrix blocks. The MPNN network includes five message-passing (MP) layers and one local coordinate message-passing (LCMP) layer. The batch size was fixed at 2, meaning that each batch contained two material structures. The loss function was set to the default value, and the learning rate was initially set to 0.001. The total training epoch was 6000. By providing the overlap matrix of the large system from the revised OPENMX code [96] and the predicted Hamiltonian from the DeepH code, the eigenvalues of the large system can be obtained by solving the eigenvalue problem [100].

3. DFT + U + V calculations

The *ab initio* evaluation of the effective electronic parameters (on-site effective Hubbard $U_{\text{eff}} = U - J$ and the intersite interaction V) and the DFT + U + V calculations are performed using the Octopus code [101,102]. A real-space spacing of 0.4 Bohr is chosen, and we employ HGH norm-conserving pseudopotentials [103]. The LDA is used for describing the local DFT part. The vacuum size, atomic coordinates, and lattice constant are taken to be the same as for the DFT treatment, as described above. In order to analyze if the system is present or not an antiferomagnetic instability when correlations are taken into account, we constructed a doubled cell by repeating the DFT unit cell along the x axis. We employed a 3×3 k-point grid for the unit cell and the 1×1 k-point grid for the double cells. The localized subspace was constructed using the Wannier90 library [104], taking the flat bands obtained from the LDA calculation performed with the Octopus code. We then populated these bands at half filling by adding an excess charge of two electrons in the system and performed DFT + U + V calculations. We performed non-polarized and spin-polarized calculations for the unit cell, as well as a spin-polarized calculations for the double cells. In all spin-polarized calculations, we started from random magnetic configurations in order to determine the ground state. Only the first nearest-neighbor interaction was considered in the intersite interaction.

The standard approach to estimate the on-site U and intersite V relies on the cRPA method. This method is, however, prohibitively expensive to be applied to twisted bilayer systems, and an alternative approach needs to be employed. In order to get a first estimate on the relative strength of the on-site and intersite interaction, we compute first the Coulomb integrals of the bare Coulomb potential.

$$\langle \phi^I_m \phi^I_m | v | \phi^J_{m'} \phi^J_{m'} \rangle = \int d\mathbf{r} d\mathbf{r}' |\phi_m(\mathbf{r})|^2 \frac{1}{|\mathbf{r} - \mathbf{r}'|} |\phi_{m'}(\mathbf{r}')|^2. \tag{A1}$$

With this approach, we get $U_{\text{bare}} = 1.99$ eV and $V_{\text{bare}} = 235$ meV, giving a ratio $U_{\text{bare}}/V_{\text{bare}} = 8.46$. While these values might seems to be very large, we can compare them to the estimate we would get for a $1s$ hydrogenic orbital of the form $\phi_{1s}(\mathbf{r}) = (Z^3/\pi)^{1/2} e^{-Zr}$, the on-site Coulomb integral $\langle \phi_{1s}\phi_{1s}|v|\phi_{1s}\phi_{1s}\rangle = \frac{5}{8}Z$. If we choose Z such that the spread of the Wannier function is the same as the spread of the Wannier state given by Wannier90 (here ≈30 Å), we obtain that $Z \approx 0.25$. This would lead to $\langle \phi_{1s}\phi_{1s}|v|\phi_{1s}\phi_{1s}\rangle \approx 4.25$ eV.

We now proceed with estimating the screened Coulomb interaction. Key to the two-dimensional materials is the change of screening compare to three-dimensional materials. To take into account the two-dimensional nature of the material, we compute the screened Coulomb integrals for the twisted bilayer system, replacing the bare Coulomb potential by the Rytova-Keldysh potential [105,106] which reads in real space

$$V_{2D}(s) = \frac{\pi}{2\rho_0}\left[H_0\left(\frac{s}{\rho_0}\right) - Y_0\left(\frac{s}{\rho_0}\right)\right], \tag{A2}$$

where H_0 and Y_0 are, respectively, the Struve and Bessel functions of the second kind and ρ_0 is a screening length, which is obtained here *ab initio* from a calculation for the untwisted bilayer calculation as explained above. In Fourier space, this potential reads

$$V_{2D}(\mathbf{q}_\parallel) = \frac{2\pi}{|\mathbf{q}_\parallel|(1+\rho_0|\mathbf{q}_\parallel|)}, \tag{A3}$$

and properly captures the asympotic behavior of the two-dimensional screening [107]. In order to determine the screening length $\rho_0 = (d\varepsilon/2)$, we use a method originally proposed by Qiu *et al.* [108] which consists in computing an effective *ab initio* screening from calculations done in a supercell

$$\varepsilon^{-1}_{2D}(q) = \frac{q}{2\pi L_z}\sum_{\mathbf{G}_z,\mathbf{G}'_z} W_{\mathbf{G}_z,\mathbf{G}'_z}(q), \tag{A4}$$

where $W_{\mathbf{G}_z,\mathbf{G}'_z}(q)$ is the usual screened Coulomb interaction, computed using the Coulomb truncation technique, as suggested in Ref. [108]. The calculation of the screened Coulomb interation $W_{\mathbf{G}_z,\mathbf{G}'_z}(q)$ was performed using the ABINIT code for the untwisted, fully relaxed, bilayer system. We used a dense 32×32 **k**-point grid, a supercell size $L_z = 24$ Å, with a cutoff energy of 13 Ha for the screening, and using 500 bands for computing the dielectric function. With this, we obtained an effective thickness $d = 35$ Å, which is a bit less than 4 times the atom-to-atom distance for the bilayer system, with the experimental value of $\varepsilon = 13.6$. This value was then used to evaluate the potential $V_{2D}(\mathbf{q}_\parallel)$ in evaluating the effective U and V for the twisted bilayer system.

In order to evaluate the Rytova-Keldysh potential with FFTs for the nonperiodic Wannier orbitals, one resort to a Coulomb integral technique. This implies to compute the Fourier transform of $V_{2D}(s)$ on a sphere of finite radius R. The analytical solution for the vanishing in-plane momentum $\mathbf{G}_\parallel = 0$ is given by $V^{\text{cutoff}}_{2D}(\mathbf{G}_\parallel = 0) = \pi^2\rho_0\{(R/\rho_0)[H_1(R/\rho_0) - Y_1(R/\rho_0)] - (2/\pi)\} \approx 2\pi R^2\{[1 - 2\gamma - 2\log(R/2\rho_0)]/4\rho_0\}$, where γ is the Euler-Mascheroni constant. The last expression is obtained using the fact that $R \ll \rho_0$ in the present work. Using the above expressions, we obtained $U = 1.448$ and $V = 0.145$ meV, leading to a ratio $U/V \sim 9.99$.

4. FRG calculations

We address electronic order beyond DFT + U + V by employing the functional renormalization group (FRG) [88] that allows to resolve particle-particle and particle-hole instabilities in an unbiased manner. We employ the static four-point truncated unity FRG (TUFRG) approximation in which the flow equations for the two-particle vertex function $\Gamma = \Gamma^{(4)}$ read

$$\partial_\Lambda \Gamma^\Lambda = \sum_\gamma \partial_\Lambda \gamma^\Lambda, \qquad \partial_\Lambda \gamma^\Lambda = \Gamma^\Lambda \circ \partial_\Lambda L^{\gamma,\Lambda} \circ \Gamma^\Lambda, \tag{A5}$$

where $\gamma \in \{P, D, C\}$ denotes the decomposition into two-particle reducible interaction channels that capture fluctuations accumulated in the particle-particle (P), direct particle-hole (D) and crossed particle-hole (C) channel. The onset of an ordered phase is signaled by the divergence of the two-particle vertex $\Gamma^{(4)}$ at a particular (critical) scale Λ_c. The leading fermionic bilinear in the divergent channel is obtained by an eigenvalue decomposition of the channel-specific vertex γ

$$\gamma_{\kappa\kappa'}(\boldsymbol{q}_\gamma) = \sum_i \phi^L_{\kappa,i}(\boldsymbol{q}_\gamma)\gamma_i(\boldsymbol{q}_\gamma)\phi^R_{\kappa',i}(\boldsymbol{q}_\gamma), \tag{A6}$$

where κ refers to the fermionic momentum variable $\boldsymbol{k}_\gamma$. The left/right eigenvectors to the channels' eigenvalues γ_i are denoted by $\phi^{L/R}_{\kappa,i}$ and give insight into the momentum structure of the order parameter. The critical scale Λ_c serves as a proxy for the critical temperature of the transition.

The FRG calculations are carried out with the TUFRG backend of the divERGe code base [109]. The flow equations are solved using an adaptive Euler integrator and the form factor expansion of the (slow) fermionic momenta $(\boldsymbol{k}_\gamma, \boldsymbol{k}'_\gamma)$ is cut off at a distance of 3.01 $|\boldsymbol{a}_M|$ in the parametrization of the vertex tensors. The bosonic momentum variable in each channel is resolved on a discrete mesh of $N_{\boldsymbol{k}} = 60\times 60$ momentum points in the Brillouin zone. An additional $N_{\boldsymbol{k}_f} = 30\times 30$ fine momentum mesh (for each coarse momentum point) is added to resolve the single-particle dispersion entering the (scaled) two-particle propagators $\partial_\Lambda L^{\gamma,\Lambda}$.

[1] J. Hubbard, *Electron correlations in narrow energy bands*, Proc. R. Soc. A **276**, 238 (1963).

[2] Junjiro Kanamori, *Electron correlation and ferromagnetism of transition metals*, Prog. Theor. Phys. **30**, 275 (1963).

[3] Martin C. Gutzwiller, *Effect of correlation on the ferromagnetism of transition metals*, Phys. Rev. Lett. **10**, 159 (1963).

[4] Efstratios Manousakis, *The spin-½ Heisenberg antiferromagnet on a square lattice and its application to the cuprous oxides*, Rev. Mod. Phys. **63**, 1 (1991).

[5] P. W. Anderson, *The resonating valence bond state in La_2CuO_4 and superconductivity*, Science **235**, 1196 (1987).

[6] V. J. Emery, *Theory of high-T_c superconductivity in oxides*, Phys. Rev. Lett. **58**, 2794 (1987).

[7] Bo-Xiao Zheng, Chia-Min Chung, Philippe Corboz, Georg Ehlers, Ming-Pu Qin, Reinhard M. Noack, Hao Shi, Steven R. White, Shiwei Zhang, and Garnet Kin-Lic Chan, *Stripe order in the underdoped region of the two-dimensional Hubbard model*, Science **358**, 1155 (2017).

[8] Edwin W. Huang, Christian B. Mendl, Hong-Chen Jiang, Brian Moritz, and Thomas P. Devereaux, *Stripe order from the perspective of the Hubbard model*, npj Quantum Mater. **3**, 22 (2018).

[9] Philip W. Phillips, Nigel E. Hussey, and Peter Abbamonte, *Stranger than metals*, Science **377**, eabh4273 (2022).

[10] Tom Timusk and Bryan Statt, *The pseudogap in high-temperature superconductors: An experimental survey*, Rep. Prog. Phys. **62**, 61 (1999).
[11] Mingpu Qin, Thomas Schäfer, Sabine Andergassen, Philippe Corboz, and Emanuel Gull, *The Hubbard model: A computational perspective*, Annu. Rev. Condens. Matter Phys. **13**, 275 (2022).
[12] Elbio Dagotto, *Correlated electrons in high-temperature superconductors*, Rev. Mod. Phys. **66**, 763 (1994).
[13] Patrick A. Lee, Naoto Nagaosa, and Xiao-Gang Wen, *Doping a Mott insulator: Physics of high-temperature superconductivity*, Rev. Mod. Phys. **78**, 17 (2006).
[14] Daniel P. Arovas, Erez Berg, Steven A. Kivelson, and Srinivas Raghu, *The Hubbard model*, Annu. Rev. Condens. Matter Phys. **13**, 239 (2022).
[15] J. P. F. LeBlanc *et al.* (Simons Collaboration on the Many-Electron Problem), *Solutions of the two-dimensional Hubbard model: Benchmarks and results from a wide range of numerical algorithms*, Phys. Rev. X **5**, 041041 (2015).
[16] Steven R. White, *Density matrix formulation for quantum renormalization groups*, Phys. Rev. Lett. **69**, 2863 (1992).
[17] Steven R. White, *Density-matrix algorithms for quantum renormalization groups*, Phys. Rev. B **48**, 10345 (1993).
[18] Antoine Georges, Gabriel Kotliar, Werner Krauth, and Marcelo J. Rozenberg, *Dynamical mean-field theory of strongly correlated fermion systems and the limit of infinite dimensions*, Rev. Mod. Phys. **68**, 13 (1996).
[19] J. E. Hirsch, *Two-dimensional Hubbard model: Numerical simulation study*, Phys. Rev. B **31**, 4403 (1985).
[20] S. R. White, D. J. Scalapino, R. L. Sugar, E. Y. Loh, J. E. Gubernatis, and R. T. Scalettar, *Numerical study of the two-dimensional Hubbard model*, Phys. Rev. B **40**, 506 (1989).
[21] Mingpu Qin, Hao Shi, and Shiwei Zhang, *Benchmark study of the two-dimensional Hubbard model with auxiliary-field quantum Monte Carlo method*, Phys. Rev. B **94**, 085103 (2016).
[22] T. A. Maier, Mark Jarrell, Thomas Pruschke, and M. Hettler, *Quantum cluster theories*, Rev. Mod. Phys. **77**, 1027 (2005).
[23] Hong-Chen Jiang and Thomas P. Devereaux, *Superconductivity in the doped Hubbard model and its interplay with next-nearest hopping t-t'*, Science **365**, 1424 (2019).
[24] Dante M. Kennes, Martin Claassen, Lede Xian, Antoine Georges, Andrew J. Millis, James Hone, Cory R. Dean, D. N. Basov, Abhay N. Pasupathy, and Angel Rubio, *Moiré heterostructures as a condensed-matter quantum simulator*, Nat. Phys. **17**, 155 (2021).
[25] Robert Jördens, Niels Strohmaier, Kenneth Günter, Henning Moritz, and Tilman Esslinger, *A Mott insulator of fermionic atoms in an optical lattice*, Nature (London) **455**, 204 (2008).
[26] Russell A. Hart, Pedro M. Duarte, Tsung-Lin Yang, Xinxing Liu, Thereza Paiva, Ehsan Khatami, Richard T. Scalettar, Nandini Trivedi, David A. Huse, and Randall G. Hulet, *Observation of antiferromagnetic correlations in the Hubbard model with ultracold atoms*, Nature (London) **519**, 211 (2015).
[27] Anton Mazurenko, Christie S. Chiu, Geoffrey Ji, Maxwell F. Parsons, Márton Kanász-Nagy, Richard Schmidt, Fabian Grusdt, Eugene Demler, Daniel Greif, and Markus Greiner, *A cold-atom Fermi-Hubbard antiferromagnet*, Nature (London) **545**, 462 (2017).
[28] Christian Gross and Immanuel Bloch, *Quantum simulations with ultracold atoms in optical lattices*, Science **357**, 995 (2017).
[29] Achintya Singha, M. Gibertini, B. Karmakar, S. Yuan, M. Polini, Giovanni Vignale, M. I. Katsnelson, A. Pinczuk, L. N. Pfeiffer, K. W. West *et al.*, *Two-dimensional Mott-Hubbard electrons in an artificial honeycomb lattice*, Science **332**, 1176 (2011).
[30] Toivo Hensgens, Takafumi Fujita, Laurens Janssen, Xiao Li, C. J. Van Diepen, Christian Reichl, Werner Wegscheider, Sankar Das Sarma, and Lieven M. K. Vandersypen, *Quantum simulation of a Fermi-Hubbard model using a semiconductor quantum dot array*, Nature (London) **548**, 70 (2017).
[31] Dave Wecker, Matthew B. Hastings, Nathan Wiebe, Bryan K. Clark, Chetan Nayak, and Matthias Troyer, *Solving strongly correlated electron models on a quantum computer*, Phys. Rev. A **92**, 062318 (2015).
[32] Stasja Stanisic, Jan Lukas Bosse, Filippo Maria Gambetta, Raul A. Santos, Wojciech Mruczkiewicz, Thomas E. O'Brien, Eric Ostby, and Ashley Montanaro, *Observing ground-state properties of the Fermi-Hubbard model using a scalable algorithm on a quantum computer*, Nat. Commun. **13**, 5743 (2022).
[33] Muqing Xu, Lev Haldar Kendrick, Anant Kale, Youqi Gang, Geoffrey Ji, Richard T. Scalettar, Martin Lebrat, and Markus Greiner, *Frustration-and doping-induced magnetism in a Fermi-Hubbard simulator*, Nature (London) **620**, 971 (2023).
[34] KS Novoselov, Artem Mishchenko, Alexandra Carvalho, and AH Castro Neto, *2D materials and van der Waals heterostructures*, Science **353**, aac9439 (2016).
[35] Max C. Lemme, Deji Akinwande, Cedric Huyghebaert, and Christoph Stampfer, *2D materials for future heterogeneous electronics*, Nat. Commun. **13**, 1392 (2022).
[36] Pablo Ares and Kostya S. Novoselov, *Recent advances in graphene and other 2D materials*, Nano Mater. Sci. **4**, 3 (2022).
[37] Soo Ho Choi, Seok Joon Yun, Yo Seob Won, Chang Seok Oh, Soo Min Kim, Ki Kang Kim, and Young Hee Lee, *Large-scale synthesis of graphene and other 2D materials towards industrialization*, Nat. Commun. **13**, 1484 (2022).
[38] Andres Castellanos-Gomez, Xiangfeng Duan, Zhe Fei, Humberto Rodriguez Gutierrez, Yuan Huang, Xinyu Huang, Jorge Quereda, Qi Qian, Eli Sutter, and Peter Sutter, *Van der Waals heterostructures*, Nat. Rev. Methods Primers **2**, 58 (2022).
[39] Yuan Cao, Valla Fatemi, Shiang Fang, Kenji Watanabe, Takashi Taniguchi, Efthimios Kaxiras, and Pablo Jarillo-Herrero, *Unconventional superconductivity in magic-angle graphene superlattices*, Nature (London) **556**, 43 (2018).
[40] Yuan Cao, Valla Fatemi, Ahmet Demir, Shiang Fang, Spencer L. Tomarken, Jason Y. Luo, Javier D. Sanchez-Yamagishi, Kenji Watanabe, Takashi Taniguchi, Efthimios Kaxiras *et al.*, *Correlated insulator behaviour at*

half-filling in magic-angle graphene superlattices, Nature (London) **556**, 80 (2018).

[41] Youngjoon Choi, Jeannette Kemmer, Yang Peng, Alex Thomson, Harpreet Arora, Robert Polski, Yiran Zhang, Hechen Ren, Jason Alicea, Gil Refael *et al.*, *Electronic correlations in twisted bilayer graphene near the magic angle*, Nat. Phys. **15**, 1174 (2019).

[42] Alexander Kerelsky, Leo J. McGilly, Dante M. Kennes, Lede Xian, Matthew Yankowitz, Shaowen Chen, K. Watanabe, T. Taniguchi, James Hone, Cory Dean *et al.*, *Maximized electron interactions at the magic angle in twisted bilayer graphene*, Nature (London) **572**, 95 (2019).

[43] Eva Y. Andrei and Allan H. MacDonald, *Graphene bilayers with a twist*, Nat. Mater. **19**, 1265 (2020).

[44] Lei Wang, En-Min Shih, Augusto Ghiotto, Lede Xian, Daniel A. Rhodes, Cheng Tan, Martin Claassen, Dante M. Kennes, Yusong Bai, Bumho Kim *et al.*, *Correlated electronic phases in twisted bilayer transition metal dichalcogenides*, Nat. Mater. **19**, 861 (2020).

[45] Yang Xu, Song Liu, Daniel A. Rhodes, Kenji Watanabe, Takashi Taniguchi, James Hone, Veit Elser, Kin Fai Mak, and Jie Shan, *Correlated insulating states at fractional fillings of moiré superlattices*, Nature (London) **587**, 214 (2020).

[46] Kin Fai Mak and Jie Shan, *Semiconductor moiré materials*, Nat. Nanotechnol. **17**, 686 (2022).

[47] Yihang Zeng, Zhengchao Xia, Kaifei Kang, Jiacheng Zhu, Patrick Knüppel, Chirag Vaswani, Kenji Watanabe, Takashi Taniguchi, Kin Fai Mak, and Jie Shan, *Thermodynamic evidence of fractional Chern insulator in moiré* $MoTe_2$, Nature (London) **622**, 69 (2023).

[48] Heonjoon Park, Jiaqi Cai, Eric Anderson, Yinong Zhang, Jiayi Zhu, Xiaoyu Liu, Chong Wang, William Holtzmann, Chaowei Hu, Zhaoyu Liu *et al.*, *Observation of fractionally quantized anomalous Hall effect*, Nature (London) **622**, 74 (2023).

[49] Fan Xu, Zheng Sun, Tongtong Jia, Chang Liu, Cheng Xu, Chushan Li, Yu Gu, Kenji Watanabe, Takashi Taniguchi, Bingbing Tong *et al.*, *Observation of integer and fractional quantum anomalous Hall effects in twisted bilayer* $MoTe_2$, Phys. Rev. X **13**, 031037 (2023).

[50] Rafi Bistritzer and Allan H. MacDonald, *Moiré bands in twisted double-layer graphene*, Proc. Natl. Acad. Sci. U.S.A. **108**, 12233 (2011).

[51] Fengcheng Wu, Timothy Lovorn, Emanuel Tutuc, and Allan H. MacDonald, *Hubbard model physics in transition metal dichalcogenide moiré bands*, Phys. Rev. Lett. **121**, 026402 (2018).

[52] Yanhao Tang, Lizhong Li, Tingxin Li, Yang Xu, Song Liu, Katayun Barmak, Kenji Watanabe, Takashi Taniguchi, Allan H. MacDonald, Jie Shan *et al.*, *Simulation of Hubbard model physics in* WSe_2/WS_2 *moiré superlattices*, Nature (London) **579**, 353 (2020).

[53] Lede Xian, Martin Claassen, Dominik Kiese, Michael M. Scherer, Simon Trebst, Dante M. Kennes, and Angel Rubio, *Realization of nearly dispersionless bands with strong orbital anisotropy from destructive interference in twisted bilayer* MoS_2, Nat. Commun. **12**, 5644 (2021).

[54] Yang Xu, Kaifei Kang, Kenji Watanabe, Takashi Taniguchi, Kin Fai Mak, and Jie Shan, *A tunable bilayer Hubbard model in twisted* WSe_2, Nat. Nanotechnol. **17**, 934 (2022).

[55] Dante M. Kennes, Lede Xian, Martin Claassen, and Angel Rubio, *One-dimensional flat bands in twisted bilayer germanium selenide*, Nat. Commun. **11**, 1124 (2020).

[56] Pengjie Wang, Guo Yu, Yves H. Kwan, Yanyu Jia, Shiming Lei, Sebastian Klemenz, F. Alexandre Cevallos, Ratnadwip Singha, Trithep Devakul, Kenji Watanabe *et al.*, *One-dimensional Luttinger liquids in a two-dimensional moiré lattice*, Nature (London) **605**, 57 (2022).

[57] Martin Claassen, Lede Xian, Dante M. Kennes, and Angel Rubio, *Ultra-strong spin-orbit coupling and topological moiré engineering in twisted* ZrS_2 *bilayers*, Nat. Commun. **13**, 4915 (2022).

[58] Lede Xian, Ammon Fischer, Martin Claassen, Jin Zhang, Angel Rubio, and Dante M. Kennes, *Engineering three-dimensional moiré flat bands*, Nano Lett. **21**, 7519 (2021).

[59] Kai Chang and Stuart S. P. Parkin, *Experimental formation of monolayer group-IV monochalcogenides*, J. Appl. Phys. **127**, 220902 (2020).

[60] Yixiu Wang, Gang Qiu, Ruoxing Wang, Shouyuan Huang, Qingxiao Wang, Yuanyue Liu, Yuchen Du, William A. Goddard III, Moon J. Kim, Xianfan Xu *et al.*, *Field-effect transistors made from solution-grown two-dimensional tellurene*, Nat. Electron. **1**, 228 (2018).

[61] Zhi-Qiang Shi, Huiping Li, Qian-Qian Yuan, Ye-Heng Song, Yang-Yang Lv, Wei Shi, Zhen-Yu Jia, Libo Gao, Yan-Bin Chen, Wenguang Zhu *et al.*, *Van der Waals heteroepitaxial growth of monolayer* Sb *in a puckered honeycomb structure*, Adv. Mater. **31**, 1806130 (2019).

[62] Zhi-Qiang Shi, Huiping Li, Cheng-Long Xue, Qian-Qian Yuan, Yang-Yang Lv, Yong-Jie Xu, Zhen-Yu Jia, Libo Gao, Yanbin Chen, Wenguang Zhu *et al.*, *Tuning the electronic structure of an α-antimonene monolayer through interface engineering*, Nano Lett. **20**, 8408 (2020).

[63] See Supplemental Material at http://link.aps.org/supplemental/10.1103/wcbz-lbr1 for additional data analysis, which includes Refs. [64–67].

[64] Wei Ku, Tom Berlijn, and Chi-Cheng Lee, *Unfolding first-principles band structures*, Phys. Rev. Lett. **104**, 216401 (2010).

[65] Voicu Popescu and Alex Zunger, *Extracting E versus* $\vec{k}$ *effective band structure from supercell calculations on alloys and impurities*, Phys. Rev. B **85**, 085201 (2012).

[66] Mattia Angeli and Allan H. MacDonald, *γ valley transition metal dichalcogenide moiré bands*, Proc. Natl. Acad. Sci. U.S.A. **118**, e2021826118 (2021).

[67] Manato Fujimoto and Toshikaze Kariyado, *Effective continuum model of twisted bilayer* GeSe *and origin of the emerging one-dimensional mode*, Phys. Rev. B **104**, 125427 (2021).

[68] Emma C. Regan, Danqing Wang, Chenhao Jin, M. Iqbal Bakti Utama, Beini Gao, Xin Wei, Sihan Zhao, Wenyu Zhao, Zuocheng Zhang, Kentaro Yumigeta *et al.*, *Mott and generalized Wigner crystal states in* WSe_2/WS_2 *moiré superlattices*, Nature (London) **579**, 359 (2020).

[69] Chun Ning Lau, Marc W. Bockrath, Kin Fai Mak, and Fan Zhang, *Reproducibility in the fabrication and physics of moiré materials*, Nature (London) **602**, 41 (2022).

[70] Carlos Forsythe, Xiaodong Zhou, Kenji Watanabe, Takashi Taniguchi, Abhay Pasupathy, Pilkyung Moon, Mikito Koshino, Philip Kim, and Cory R. Dean, *Band structure engineering of 2D materials using patterned dielectric superlattices*, Nat. Nanotechnol. **13**, 566 (2018).

[71] Heribert Wiedemeier, Hans Georg, and Georg von Schnering, *Refinement of the structures of* GeS, GeSe, SnS and SnSe, Z. Kristallogr.-Cryst. Mater. **148**, 295 (1978).

[72] Nicolas Mounet, Marco Gibertini, Philippe Schwaller, Davide Campi, Andrius Merkys, Antimo Marrazzo, Thibault Sohier, Ivano Eligio Castelli, Andrea Cepellotti, Giovanni Pizzi *et al.*, *Two-dimensional materials from high-throughput computational exfoliation of experimentally known compounds*, Nat. Nanotechnol. **13**, 246 (2018).

[73] Likai Li, Jonghwan Kim, Chenhao Jin, Guo Jun Ye, Diana Y. Qiu, Felipe H. Da Jornada, Zhiwen Shi, Long Chen, Zuocheng Zhang, Fangyuan Yang *et al.*, *Direct observation of the layer-dependent electronic structure in phosphorene*, Nat. Nanotechnol. **12**, 21 (2017).

[74] Shilong Zhao, Erqing Wang, Ebru Alime Üzer, Shuaifei Guo, Ruishi Qi, Junyang Tan, Kenji Watanabe, Takashi Taniguchi, Tom Nilges, Peng Gao *et al.*, *Anisotropic moiré optical transitions in twisted monolayer/bilayer phosphorene heterostructures*, Nat. Commun. **12**, 3947 (2021).

[75] Shuaifei Guo, Mingyan Luo, Gang Shi, Ning Tian, Zhe Huang, Fangyuan Yang, Liguo Ma, Nai Zhou Wang, Qinzhen Shi, Kailiang Xu *et al.*, *An ultra-high vacuum system for fabricating clean two-dimensional material devices*, Rev. Sci. Instrum. **94** (2023).

[76] Wendong Wang, Nicholas Clark, Matthew Hamer, Amy Carl, Endre Tovari, Sam Sullivan-Allsop, Evan Tillotson, Yunze Gao, Hugo de Latour, Francisco Selles *et al.*, *Clean assembly of van der Waals heterostructures using silicon nitride membranes*, Nat. Electron. **6**, 981 (2023).

[77] C. N. Varney, C.-R. Lee, Z. J. Bai, S. Chiesa, M. Jarrell, and R. T. Scalettar, *Quantum Monte Carlo study of the two-dimensional fermion Hubbard model*, Phys. Rev. B **80**, 075116 (2009).

[78] Daniel F. Agterberg, J. C. Séamus Davis, Stephen D. Edkins, Eduardo Fradkin, Dale J. Van Harlingen, Steven A. Kivelson, Patrick A. Lee, Leo Radzihovsky, John M. Tranquada, and Yuxuan Wang, *The physics of pair-density waves: Cuprate superconductors and beyond*, Annu. Rev. Condens. Matter Phys. **11**, 231 (2020).

[79] E. Berg, E. Fradkin, E.-A. Kim, S. A. Kivelson, V. Oganesyan, J. M. Tranquada, and S. C. Zhang, *Dynamical layer decoupling in a stripe-ordered high-T_c superconductor*, Phys. Rev. Lett. **99**, 127003 (2007).

[80] Patrick A. Lee, *Amperean pairing and the pseudogap phase of cuprate superconductors*, Phys. Rev. X **4**, 031017 (2014).

[81] Mingpu Qin, Chia-Min Chung, Hao Shi, Ettore Vitali, Claudius Hubig, Ulrich Schollwöck, Steven R. White, Shiwei Zhang, and (Simons Collaboration on the Many-Electron Problem), *Absence of superconductivity in the pure two-dimensional Hubbard model*, Phys. Rev. X **10**, 031016 (2020).

[82] Kota Ido, Takahiro Ohgoe, and Masatoshi Imada, *Competition among various charge-inhomogeneous states and d-wave superconducting state in Hubbard models on square lattices*, Phys. Rev. B **97**, 045138 (2018).

[83] Luca F. Tocchio, Arianna Montorsi, and Federico Becca, *Metallic and insulating stripes and their relation with superconductivity in the doped Hubbard model*, SciPost Phys. **7**, 021 (2019).

[84] Andrew S. Darmawan, Yusuke Nomura, Youhei Yamaji, and Masatoshi Imada, *Stripe and superconducting order competing in the Hubbard model on a square lattice studied by a combined variational Monte Carlo and tensor network method*, Phys. Rev. B **98**, 205132 (2018).

[85] Boris Ponsioen, Sangwoo S. Chung, and Philippe Corboz, *Period 4 stripe in the extended two-dimensional Hubbard model*, Phys. Rev. B **100**, 195141 (2019).

[86] Hao Xu, Chia-Min Chung, Mingpu Qin, Ulrich Schollwöck, Steven R. White, and Shiwei Zhang, *Coexistence of superconductivity with partially filled stripes in the Hubbard model*, Science **384**, eadh7691 (2024).

[87] Yi-Fan Jiang, Jan Zaanen, Thomas P. Devereaux, and Hong-Chen Jiang, *Ground state phase diagram of the doped Hubbard model on the four-leg cylinder*, Phys. Rev. Res. **2**, 033073 (2020).

[88] W. Metzner, M. Salmhofer, C. Honerkamp, V. Meden, and K. Schonhammer, *Functional renormalization group approach to correlated fermion systems*, Rev. Mod. Phys. **84**, 299 (2012).

[89] C. Platt, W. Hanke, and R. Thomale, *Functional renormalization group for multi-orbital Fermi surface instabilities*, Adv. Phys. **62**, 453 (2013).

[90] P. Myles Eugenio, Zhu-Xi Luo, Ashvin Vishwanath, and Pavel A. Volkov, *Tunable $t - t' - u$ Hubbard models in twisted square homobilayers*, Phys. Rev. Lett. **134**, 236503 (2025).

[91] Georg Kresse and Jürgen Furthmüller, *Efficient iterative schemes for ab initio total-energy calculations using a plane-wave basis set*, Phys. Rev. B **54**, 11169 (1996).

[92] Peter E. Blöchl, *Projector augmented-wave method*, Phys. Rev. B **50**, 17953 (1994).

[93] John P. Perdew, Kieron Burke, and Matthias Ernzerhof, *Generalized gradient approximation made simple*, Phys. Rev. Lett. **77**, 3865 (1996).

[94] Alexandre Tkatchenko and Matthias Scheffler, *Accurate molecular van der Waals interactions from ground-state electron density and free-atom reference data*, Phys. Rev. Lett. **102**, 073005 (2009).

[95] He Li, Zun Wang, Nianlong Zou, Meng Ye, Runzhang Xu, Xiaoxun Gong, Wenhui Duan, and Yong Xu, *Deep-learning density functional theory Hamiltonian for efficient ab initio electronic-structure calculation*, Nat. Comput. Sci. **2**, 367 (2022).

[96] T. Ozaki, H. Kino, J. Yu *et al.*, *Open source package for material explorer*, http://www.openmx-square.org (2019).

[97] I. Morrison, D. M. Bylander, and L. Kleinman, *Nonlocal Hermitian norm-conserving vanderbilt pseudopotential*, Phys. Rev. B **47**, 6728 (1993).

[98] Stefan Grimme, Jens Antony, Stephan Ehrlich, and Helge Krieg, *A consistent and accurate ab initio parametrization*

of density functional dispersion correction (DFT-D) for the 94 elements H – Pu, J. Chem. Phys. **132** (2010).

[99] Matthias Fey and Jan Eric Lenssen, *Fast graph representation learning with PyTorch geometric*, arXiv:1903.02428.

[100] Chong Wang, Sibo Zhao, Xiaomi Guo, Xinguo Ren, Bing-Lin Gu, Yong Xu, and Wenhui Duan, *First-principles calculation of optical responses based on nonorthogonal localized orbitals*, New J. Phys. **21**, 093001 (2019).

[101] Nicolas Tancogne-Dejean, Micael J. T. Oliveira, Xavier Andrade, Heiko Appel, Carlos H. Borca, Guillaume Le Breton, Florian Buchholz, Alberto Castro, Stefano Corni, Alfredo A. Correa *et al.*, *Octopus, a computational framework for exploring light-driven phenomena and quantum dynamics in extended and finite systems*, J. Chem. Phys. **152**, 124119 (2020).

[102] Nicolas Tancogne-Dejean, Micael J. T. Oliveira, and Angel Rubio, *Self-consistent* dft + u *method for real-space time-dependent density functional theory calculations*, Phys. Rev. B **96**, 245133 (2017).

[103] C. Hartwigsen, S. Goedecker, and J. Hutter, *Relativistic separable dual-space Gaussian pseudopotentials from H to* Rn, Phys. Rev. B **58**, 3641 (1998).

[104] G. Pizzi *et al.*, *Wannier90 as a community code: New features and applications*, J. Phys. Condens. Matter **32**, 165902 (2020).

[105] Natalia S. Rytova, *Screened potential of a point charge in a thin film*, arXiv:1806.00976.

[106] LV Keldysh, *Coulomb interaction in thin semiconductor and semimetal films*, in *Selected Papers of Leonid V Keldysh* (World Scientific, Singapore, 2024), pp. 155–158.

[107] Pierluigi Cudazzo, Ilya V. Tokatly, and Angel Rubio, *Dielectric screening in two-dimensional insulators: Implications for excitonic and impurity states in graphane*, Phys. Rev. B **84**, 085406 (2011).

[108] Diana Y. Qiu, Felipe H. da Jornada, and Steven G. Louie, *Screening and many-body effects in two-dimensional crystals: Monolayer* MoS_2, Phys. Rev. B **93**, 235435 (2016).

[109] Jonas Profe, Dante M. Kennes, and Lennart Klebl, *divERGe implements various exact renormalization group examples*, SciPost Phys. Codebases 026 (2024).

Correction: A grant number in the Acknowledgments contained an error and has been fixed.